2018 IEEE International Conference on Robotics and Automation (ICRA)
May 21-25, 2018, Brisbane, Australia

Design, Modeling and Control of a 2-DoF Robotic Guidewire

Yash Chitalia*, Xuefeng Wang and Jaydev P. Desai, Fellow, IEEE

***Abstract*— In most cases of peripheral arterial disease (PAD), the operating surgeon must use a variety of catheters riding on a thin wire known as a 'guidewire'. This guidewire must be manually navigated through a tortuous pathway of arteries to arrive at the diseased area. Automation of the guidewire therefore reduces surgeon effort and minimizes the time required for a PAD procedure, but is restricted by the size constraints of a standard guidewire. This work presents the design of a robotically actuated 2 degree-of-freedom (DoF) guidewire tip comprised of joints laser micro-machined into a 0.78 mm (< 2.4 Fr) Nitinol tube. We present an analysis of the notch joint used as a building block in the robot and a control strategy for this type of a joint. The experimental results show that tendon force is an important observable quantity that can be used as a shape sensing mechanism for this type of a joint in practical control applications.**

I. Introduction

Peripheral artery disease (PAD) is one of the most common causes of cardiovascular deaths in the world, with an estimated 202 million people suffering from it in 2010 [1]. It is caused by the deposition of calcium, lipids and cholesterol in the arteries at the lower extremities of the body. Atherectomy is a minimally invasive procedure used commonly to treat PAD. In this procedure, to gain access to the diseased artery, the physician usually makes an incision into the femoral artery of the healthy leg [2]. A soft guidewire with a slightly bent tip is then inserted into the healthy artery and navigated to the diseased artery by crossing the aortic bifurcation. Following this navigation, a variety of catheters are inserted so that they ride on the guidewire. These catheters may be equipped with either the tools to perform the atherectomy such as a micro-drill, or a drug delivery unit (in the form of a drug coated balloon) to help prevent further deposition on that artery. Presently, the physician manually maneuvers the guidewire to the target artery by insertion, retraction and rotation of the wire base, while observing its movement on a real-time fluoroscopic image. Such dexterous navigation of the guidewire tip under two-dimensional visual feedback is difficult and time consuming and requires significant experience [3]. In this work, we propose a novel design for a robotic guidewire tip with two orthogonally oriented asymmetric notch joints, that offer 2 degrees-of-freedom to the guidewire tip. This expands the workspace of the guidewire and provides the physician with the ability to navigate at the distal end, to go around a plaque or other structures, such as a vessel bifurcation along the path.

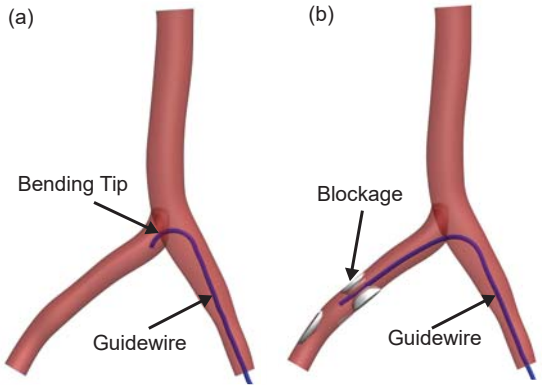

Fig. 1: (a) A guidewire is navigated through tortuous arterial pathways such as the aortic bifurcation. (b) A guidewire must also be navigated around blockages in the arteries before catheters are inserted to clear the blockages.

The non-robotic guidewires commercially available range in their outer diameters from 0.3556 mm (∼1.06 Fr) to 0.889 mm (∼2.7 Fr), which makes miniaturization an important requirement while designing a robotic guidewire tip. In general, micro-scale catheters use five types of actuation strategies to control the tip of the catheters: thermal, pressure-based, magnetic, electrical and mechanical (tendon-driven or concentric) [4]. In this work, we use mechanical actuation, using a design feature called an *asymmetric notch* as a building block to construct our multi-DoF robotic guidewire tip. The notion of a uni-directional asymmetric notch joint has been investigated and analyzed by [5], [6]. In this work, we propose an asymmetric design that allows an increased range of motion than in previous work, in that it allows the joint to be controlled in both directions in the plane of the notches. Using this design as an elementary unit, we construct a 2 DoF robot using a NiTi superelastic tube of outer diameter 0.78 mm (< 2.4 French). A full kinematic analysis of this robot is presented in this work to relate joint curvatures and Cartesian coordinates.

We follow this with a static analysis of each of the joints that form our robot, and explore a basic control strategy for the base joint of our robot. Loschak et al [7] make use of analytical inverse kinematics for higher level joint space control, followed by minor adjustments using differential kinematics in the position feedback loop. This control loop was used as a component in a proportional controller to adjust the roll angle of a commercially available ultrasound catheter. In [8], the authors used an Extended Kalman Filter to predict target values for the ultrasound catheter in the presence of respiratory disturbances, and used a PID loop

Y. Chitalia, X. Wang and J. P. Desai are with the Medical Robotics and Automation (RoboMed) Laboratory, Wallace H. Coulter Department of Biomedical Engineering, Georgia Institute of Technology, Atlanta, Georgia.
*Y. Chitalia is the corresponding author {yashc@gatech.edu}.
The authors would like to thank Mr. Richard Shafer and Mr. Jun Sheng for their help with machining the guidewires as well as Resonetics Corporation for providing us with some of the machined samples.
Disclosure Statement: Dr. Jaydev P. Desai and Mr. Yash Chitalia are co-inventors of this technology and the intent is to commercialize it.

to control the distal end of the catheter. Velocity control is also an option for continuum robots [9], [10], where the Jacobian of the robot is used to link joint-space and task-space velocities, and integrated to arrive at actuator-space parameters that control the robot. Our design is modeled with an approach similar to the one used by Camarillo et al. in [11], [12], which incorporates and accounts for inter-joint load-coupling to control each DoF independently. This is done so that we can integrate load-coupling into our model for full 2-DoF control in the future, while using the feedback controller we have proposed in this work.

A variety of techniques are being used presently to estimate the shape of a continuum manipulator as feedback to a closed loop control system, including silhouette detection [13], X-ray image-processing [14] and fiber Bragg grating sensors [15], [16]. Due to the size constraints of a guidewire, shape sensing as a form of feedback for the control system becomes a challenging problem. In this work, we present a novel observer that makes use of the tension felt at the point where the tendons are bonded to the actuators as feedback to the control system. Due to this non-localized shape estimation technique, we must model the effects of friction caused by tendon routing into our control strategy.

This work can be summarized as follows: We begin by introducing the design of the robotic guidewire, and the manufacturing process for the same (Sec. II-A). Section II-B presents an analysis of the kinematics of the robot, followed by the development of a static model for the notch joint (Section III-A) and the base joint which includes the effects of tendon routing friction (Section III-B). We address the issue of inter-joint load-coupling in Section III-C, and propose a strategy for correcting it in open-loop. Finally, we validate our static model using an observer that estimates shape of the base joint using tendon tension (Section IV), and present tracking results for several task space trajectories in Section IV-B.

II. Robot Design and Modeling

In this section, we define the guidewire tip as a 2 DoF robot and present the design decisions made in building this robot, followed by a general kinematics model of the robot.

A. Design and Construction

The robot presented in this work is tendon driven, and contains two degrees-of-freedom. Each degree-of-freedom is controlled by two tendons that permit the joint to be controlled bi-directionally. Each pair of tendons controlling a joint is attached to the distal end of that joint. As a result, a total of four tendons are routed through the inner lumen of the robot (see Fig. 2 (top, inset)) The design of the robot is detailed in Fig. 2 (bottom). As can be seen in this figure, the robot is constructed from a single tube of Nitinol by etching notches into the tube. To manufacture the above designs, an Infrared Femtosecond Laser (Resonetics Corporation, Massachusetts, United States) was used to cut rectangular notches into a NiTi tube of an outer diameter of 0.78 mm and inner diameter of about 0.62 mm (Confluent

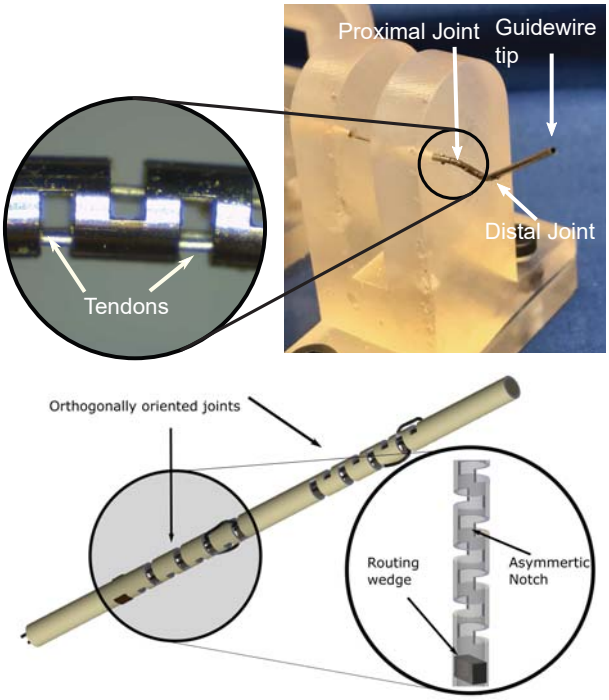

Fig. 2: (top) Image of the two joints of the robotic guidewire. The orthogonally oriented distal joint is seen to the right of the image and the inset shows the tendons passing through the joint, (bottom) Schematic of the 2-DoF micro-scale robot using orthogonally oriented notches. The inset shows the schematic of the base joint, along with the routing wedge.

Medical, California, United States). The raw Nitinol tube is placed in a lathe chuck to permit the rotation of the tube between the etching of joints, thus allowing the finished robot body to be constructed without physically extracting the part from the laser, thus minimizing positioning errors. The usage of femtosecond laser pulses minimizes the heat-affected zone (HAZ) around the notches, therefore allowing the micromachining process to occur without accidental treatment of the material. This is not necessarily true for other manufacturing processes such as milling [5] or ablation with a laser of a longer pulse-width.

The creation of notches in the Nitinol tube permits the tube to be bent in the plane of the notches, thus creating a joint at the location of the notches (Fig. 2, bottom). By rotating the tube between joints, we are able to modify the orientation of these joints. For the purpose of this work, we rotate the raw tube by $\frac{\pi}{2}$ between joints, thus orienting the joints orthogonal to each other (see Fig. 2). Finally, NiTi tendons with 0.1 mm diameter (Confluent Medical, California, United States) are manually routed into the tube and the ends bonded to the outer walls of the Nitinol tube. We assume that a positive tension is applied to these tendons when they are pulled, and the tendons are incapable of exerting a negative tension on the tube. Also, we make the assumption, that the tendons exert a point force at their attachment point at the inner wall of the tube, and a constant reaction force along the wall of the tube [11].

To minimize coupling between the joints, tendon-driven continuum robots often use a variety of load decoupling strategies. These may include routing the tendons through

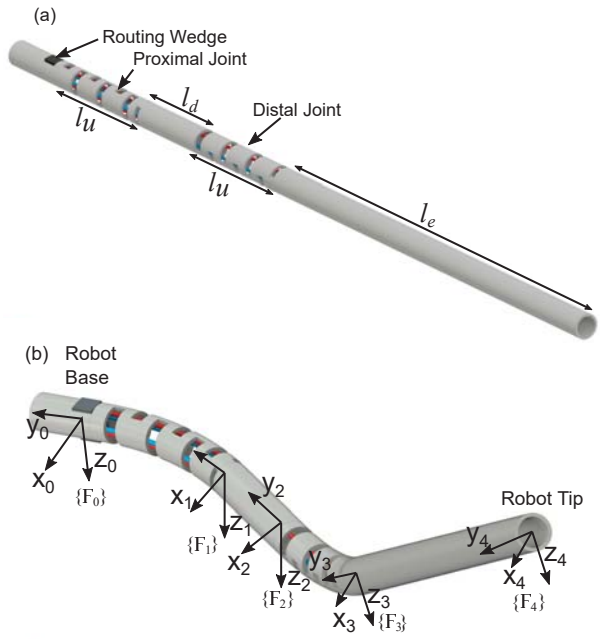

Fig. 3: Forward kinematic model of a notch joint (a) Undeformed model with joint lengths, (b) Robotic guidewire tip in a deformed state with frames $\{F_0\}$-$\{F_4\}$ attached to the central axis of the robot.

an inner spine [17] or through individual channels [12], [18]. In our case, we are unable to do either, due to the lack of space in the inner lumen of the Nitinol tube. As a result, we forfeit the notion of complete load-decoupling of the tendons, and instead strive to achieve a 'controlled load-coupling' of the tendons through the inner lumen. This is achieved by inserting a rigid Nitinol strip (termed the *routing wedge* in Fig. 2 (bottom)). As seen in Fig. 2 (top), one tendon of the proximal joint and one tendon of the distal joint are routed through each of the two openings of the routing strip. As a result, we achieve a repeatable inter-joint load-coupling in the robot, while keeping the manufacturing cost of the robot low. More complex routing mechanisms would be able to achieve a lower level of load-coupling between the proximal and distal joints, but would result in a longer manufacturing times. In this work, we hope to initiate a framework, that helps us easily incorporate our load-coupling into our control strategy (the analysis of this coupling and control strategies for the same will be provided in future work).

B. Joint and Robot Model

In this work, we model each asymmetric-notch joint of our underactuated robot as having a piecewise-constant curvature, which enables ease of robot-independent kinematic transformations [19]. In this section we begin by recapping an inverse transformation from the task space of the robot ($\boldsymbol{y}$) to the configuration space parameters ($\boldsymbol{\kappa}$), which is robot independent. Once this transformation is defined, we can move to the actuator space of the robot via a consideration of the statics of the model [12].

The dimensions associated with the kinematics of the robot are defined in Fig. 3 (a), and the associated frames are denoted in Fig. 3 (b). We denote the initial (undeformed) length of each notch joint by l_u. When the proximal joint is actuated by the tendon, it deforms by an angle θ. The curvature of this joint is defined as $\kappa_1 = \frac{\theta}{l_u}$, and the homogeneous transformation matrix for this joint is given as,

$$B_1^0 = \begin{bmatrix} C_\theta & -S_\theta & 0 & \frac{1-cos\theta}{\kappa_1} \\ S_\theta & C_\theta & 0 & -\frac{sin\theta}{\kappa_1} \\ 0 & 0 & 1 & 0 \\ 0 & 0 & 0 & 1 \end{bmatrix} \tag{1}$$

where C and S denote the cosine and sine functions, respectively. Unlike most continuum manipulators that have co-located DoFs, the second degree-of-freedom of our manipulator is located is a certain distance l_d from $\{F_1\}$. This degree-of-freedom allows the robot to move out of the x_0-y_0 plane by an angle φ and its curvature is defined as $\kappa_2 = \frac{\varphi}{l_u}$. Therefore, the final transformation to the base of the robot from the tip can be formulated as follows:

$$B_4^0 = B_1^0.B_2^1.B_3^2.B_4^3 \tag{2}$$

where,

$$B_2^1 = \begin{bmatrix} 1 & 0 & 0 & 0 \\ 0 & 1 & 0 & -l_d \\ 0 & 0 & 1 & 0 \\ 0 & 0 & 0 & 1 \end{bmatrix} \tag{3}$$

and B_3^2 takes us from $\{F_3\}$ to $\{F_2\}$,

$$B_3^2 = \begin{bmatrix} 1 & 0 & 0 & 0 \\ 0 & C_\varphi & -S_\varphi & -\frac{sin\varphi}{\kappa_2} \\ 0 & S_\varphi & C_\varphi & \frac{cos\varphi-1}{\kappa_2} \\ 0 & 0 & 0 & 1 \end{bmatrix} \tag{4}$$

Finally, B_4^3 involves a simple translation from $\{F_4\}$ to $\{F_3\}$, along $-y_3$ by length l_e. Ignoring the orientation at the tip of the guidewire, and assuming a given task-space reference input $[p^0, 1]^T \in \mathbb{R}^4$,

$$\begin{bmatrix} p^0 \\ 1 \end{bmatrix} = B_4^0 \cdot \begin{bmatrix} o^4 \\ 1 \end{bmatrix} \tag{5}$$

where $o^4 \in \mathbb{R}^3$ is the origin in the $\{F_4\}$.

For the controller to follow predefined trajectories, we must first define the inverse kinematics of the guidewire. Eq. 5 results in the following equations,

$$p_x^0 = l_e \sin\theta\cos\varphi + \frac{\sin\theta\sin\varphi}{\kappa_2} + l_d\sin\theta + (\frac{1-\cos\theta}{\kappa_1}) \tag{6}$$

and subsequently,

$$p_z^0 = -l_e \cdot \sin\theta + (\frac{\cos\varphi - 1}{\kappa_2}) \tag{7}$$

The two unknowns θ and φ, and therefore, the curvatures (κ_1, κ_2) can be derived numerically using the above equations [20], [21]. We assume that the initial values of the joint angles are $\theta_{inital} = \arctan(\frac{p_x^0}{2l_u+l_d+l_e})$ and $\varphi_{intial} = \arctan(\frac{p_z^0}{l_u+l_e})$, so that $\theta_{initial} \leq \theta$ and $\varphi_{intial} \leq \varphi$, and increment joint angles until we converge upon the correct values. We use this approach to arrive at the robot curvature for our control system discussed in Section IV.

III. Joint Kinematics and Statics

In addition to the geometric kinematics discussed above, a sufficient understanding of each notch joint comprising the robot must be developed. This includes a mapping from the joint curvature to the tension applied at the base of the joint. Traditionally, a mapping from the configuration space (κ) to the actuator space parameters ($\mathbf{u}$) is considered. However, in our case, we notice that there is a large variance introduced in this relationship by extremely small changes in the tendon path through the lumen of the tube especially at the point where it is bonded to the wall of the NiTi tube. On the other hand, the tension-curvature relationship is more repeatable and consistent, and we will derive the same in this section. For this set of trials, we consider only the case of a single tendon routed straight to distal end of the base joint of the robot.

A. Moment-Curvature Relationship

The bending angle of the entire notch joint results from the deformation of each notch that is formed by two tubes and a curved wall. A simplified linear static model of the curved wall and tubes will be demonstrated in our future work. The total joint curvature κ of the joint can be approximated by superposition of bending angles of all individual tubes in the notch, which indicates a linear relationship between the curvature κ and tendon force P:

$$\kappa = d \cdot E_b \cdot P \tag{8}$$

where E_b can be defined as the bending elasticity of the joint [11]. Althought the analytical model above can provide a theoretical explaination about the bending behavior of the notch joint, an accurate value of E_b can be esimated from experiments presented later in this paper.

B. Friction Effects

The above moment-curvature relations were developed with a setup that was designed assuming negligible friction effects. However, in a realistic situation, where two tendons are attached to the notch joint, and are not directly routed to the attachment point, we would see the effects of friction in this relationship. Due to the small diameter of the robot and the tendons controlling the robot, tendon tension can be measured only at the attachment point of the tendons to the actuators. As a result, friction must be incorporated into the moment-curvature relationship defined above. We use a Coulomb friction model to estimate the relationship between the measured tendon tension (τ) and the tension applied at base of the notch joint (T),

$$\tau = T \cdot e^{\mu \cdot \alpha \cdot \text{sgn}(v)} \tag{9}$$

where μ is the coefficient of friction of the routing channel, α is the wrapping angle and v is the tendon velocity. Therefore, the relationship between the sensed tension and the joint curvature is given by,

$$\kappa = E_b \cdot \frac{d \cdot \tau}{e^{\mu \cdot \alpha \cdot \text{sgn}(v)}} \tag{10}$$

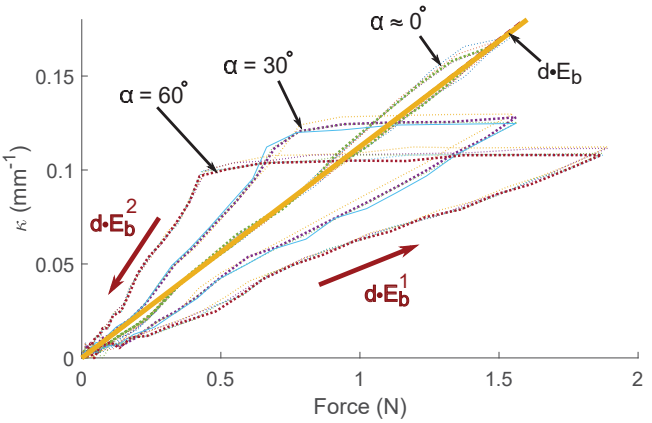

Fig. 4: Hysteresis seen in the τ vs. κ relationships for various values of wrapping angle (α) helps in estimating coefficient of friction (μ) and the bending elasticity (E_b) of the base joint.

The hysteresis in Fig. 4 for differing values of wrapping angle displays a linear τ - κ relationship for both positive and negative values of v. The slopes of these linear curves can therefore be expressed as $\Gamma_b(v, \alpha) = \frac{d \cdot E_b}{e^{\mu \cdot \alpha \cdot \text{sgn}(v)}}$. For the hysteresis loop of angle α, we therefore can define two slopes E_b^1, and E_b^2, as displayed in Fig. 4. Assuming $E_b^1 = \frac{d \cdot E_b}{e^{\mu \cdot \alpha}}$ and $E_b^2 = \frac{d \cdot E_b}{e^{-\mu \cdot \alpha}}$.

Since the slopes E_b^1, E_b^2 are known, we can extract the value of E_b as

$$E_b = \frac{\sqrt{E_b^1 \cdot E_b^2}}{d} \tag{11}$$

We can see in Fig. 4, that for various wrapping angles, this value of joint bending elasticity (E_b) stays constant. As we specified previously, each joint of the robot has two tendons attached to its distal end for bidirectional control. As a result, we will have two wrapping angle values (α_1, α_2) associated with the base joint of the robot.

C. Coupling Effects

Due to the tendon routing described previously, distal tendons impart a moment on the proximal joint, causing an inter-joint load-coupling [12] to exist by design. In the absence of such coupling, actuating the distal joint without any actuation of the proximal joint should only cause the tip of the robot to move in the $y_0 - z_0$ plane. As a result, a projection of the robot tip on the $x_0 - z_0$ plane should result only in motion along the z_0 axis. However, we observed that a projection of the robot tip on the $x_0 - z_0$ plane results in motion along both the axes (see Fig. 5 (left), solid line). This phenomenon was also noted when the proximal joint was pre-bent to a non-zero value of joint angle ($\theta \neq 0$) (see Fig. 5 (left), dashed lines). This clearly shows, that pure actuation of the distal joint also causes additional bending in the proximal joint. In order to model the inter-joint coupling, we modify Eq. 8 as follows:

$$\underbrace{\begin{bmatrix}\kappa_1 \\ \kappa_2\end{bmatrix}}_{\kappa} = d \cdot \underbrace{\begin{bmatrix}1 & 1 \\ 0 & 1\end{bmatrix}}_{C} \cdot \underbrace{\begin{bmatrix}E_b & 0 \\ 0 & E_b\end{bmatrix}}_{E_{bending}} \cdot \underbrace{\begin{bmatrix}T_1 \\ T_2\end{bmatrix}}_{T} \tag{12}$$

where T_i is the tension applied at the base of the joint i.

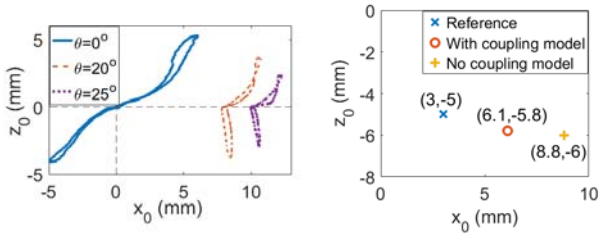

Fig. 5: (left) Projection of robot tip on $x_0 - z_0$ plane indicates coupling seen between the two DoFs of the guidewire; (right) Use of a coupling model minimizes the steady state error in 2-DoFs.

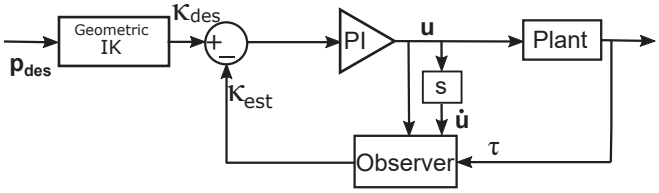

Fig. 6: Closed loop control system to perform position control on the guidewire base-joint-space variables.

This relationship can be used to place the tip in the 2-DoF space, as shown in Fig. 5 (right). A coupling model improves the steady-state error in 2 DoFs, where the Euclidean norm of the error decreases from 6.1 mm to 3.2 mm. In our future work, we plan to develop a more complete model of the coupling effect, and address problems like load-decoupled closed-loop control and path planning.

IV. Control System

In this section, we initiate the design of a controller to take advantage of the moment-curvature relationship defined previously to control the base joint of the robot. For the purpose of this paper, we define the task space as the x_0-z_0 plane (while the operational space [22] of the robot is still $\mathbb{R}^6$). The proposed controller for this task space trajectory control of the robot tip is shown in Fig. 6. Consecutive points along a trajectory in the x_0-z_0 plane are provided as input (p_{des}) to the Geomertic Inverse Kinematics algorithm defined in Section II-B. This computation results in a desired curvature κ_{des}, that is then compared with the output of an observer that outputs the most recent state estimate κ_{est}. A PI controller for the actuator displacement is designed as $\mathbf{u} = K_p e + K_i \int e dt$, where $e = (\kappa_{des} - \kappa_{est})$.

A. Observer Design

The Observer Block in Fig. 6 is designed to use the moment-curvature relationships to estimate the shape of the robot. Using the friction model defined in Section III-B, we design a piecewise linear observer that uses the following relationships to estimate the base joint curvature $\kappa_{est}[\mathrm{n}]$ at the n^{th} discrete time step,

$$\kappa_{est}[\mathrm{n}] = \begin{cases} d \cdot \Gamma_{piecewise}(\mathbf{u}, \dot{\mathbf{u}}, \mathrm{n}) \cdot \tau[\mathrm{n}], \text{ if } \operatorname{sgn}(\dot{\mathbf{u}}[\mathrm{n}]) \\ \qquad\qquad\qquad\qquad = \operatorname{sgn}(\dot{\mathbf{u}}[\mathrm{n}-1]) \\ \kappa_{est}[\mathrm{n}-1], \text{ else if } \tau[\mathrm{n}] \in [\tau_{min}, \tau_{max}] \\ d \cdot \Gamma_{piecewise}(\mathbf{u}, \dot{\mathbf{u}}, \mathrm{n}) \cdot \tau[\mathrm{n}], \text{ else.} \end{cases}$$

Here, $[\tau_{min}, \tau_{max}]$ which is the range of forces, for which the hysteresis curve plateaus is computed at each point in time. Also, the bending elasticity function $\Gamma_{piecewise}(\mathbf{u}, \dot{\mathbf{u}}, n)$ is different from the term Γ_b defined previously, and can be defined as follows:

$$\Gamma_{piecewise}(\mathbf{u}, \dot{\mathbf{u}}, \mathrm{n}) = \begin{cases} \Gamma_b(\alpha_1, \dot{\mathbf{u}}), \text{ if } \operatorname{sgn}(\mathbf{u}[\mathrm{n}]) > 0 \\ \Gamma_b(\alpha_2, \dot{\mathbf{u}}), \text{ else} \end{cases}$$

Where α_i is the wrapping angle of the tendon that is currently engaged. We tested our observer by providing a set of random trajectories to the system while sampling the curvature under a microscope at several points (See Fig. 7). Using this observer, a satisfactory estimate of the base joint curvature in either direction is obtained, and may be used as feedback in our control system.

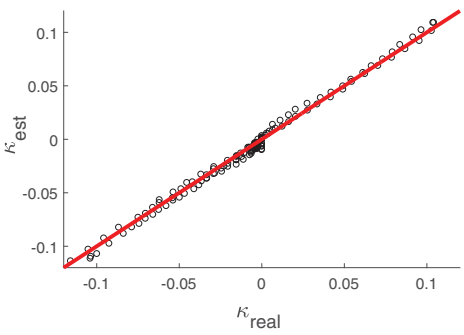

Fig. 7: Plot of Ground Truth curvature (κ_{real}) vs. the estimate curvature by our observer(κ_{est})), sampled during a set of random trajectories provided to the system. R^2 value for the estimate value of curvature was found to be 99.29%.

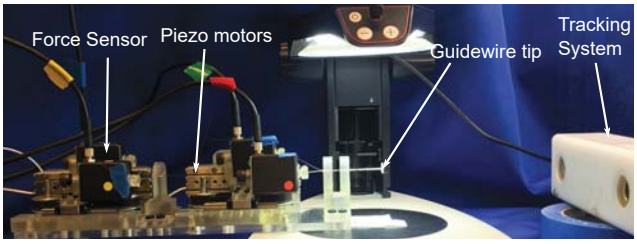

Fig. 8: Antagonistic motion-based controller hardware to test tracking accuracy. A tracker connected to the end of the guidewire prototype helps track the tip position in the $x_0 - z_0$ plane.

B. Tracking Performance

To test our controller, we constructed the compact setup shown in Fig. 8. Each joint of the robot has two tendons bonded to its distal end, which on the actuator side terminate at an antagonistic transmission which uses a single piezo-based linear actuator (SmarAct GmbH, Oldenburg, Germany). The transmission consists of a timing-belt and pulley arrangement that enables antagonistic motion of the two tendons in effect, similar to the ones used in previous robotic catheter controllers [20]. Each tendon is bonded to the transmission via a load cell with a maximum load capacity of 5 lbs (Transducer Techniques, California, United States). The data from the force sensor, an encoder and the microscope are acquired via a 16-bit ADC (Model 826, Sensoray, Portland, United States) and UART respectively. An image processing algorithm that uses Hough transforms automatically provides us with the ground truth for the base joint curvature at each point of time. Lastly, a marker is attached to tip, and a

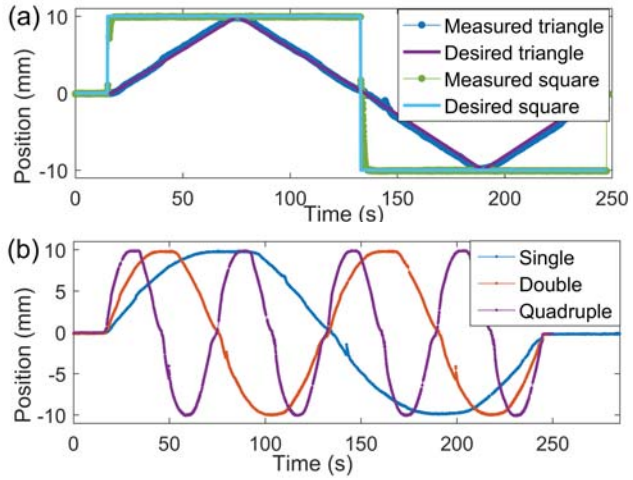

Fig. 9: (a) Tracking results of the base joint for triangular and square reference inputs on the x_0 axis, (b) Tracking results for sinusoids of varying frequencies.

stereoscopic camera (MicronTracker H40, Toronto, Ontario, Canada) tracks the end of the guidewire prototype in the x_0-z_0 plane.

Next, we provided three types of input profiles (sinusoidal, triangular and square trajectories) in task space to the base joint controller. The time period of each input type was varied from 50 secs - 250 secs. Fig. 9(a)-(b) illustrates that the PI controller defined previously is able to track the input profiles closely, with negligible steady state error for each step input. Furthermore, it is also able to track at speeds often seen in a surgical environment.

V. Conclusions and Future Work

In this work, we present a novel robotically actuated 2-DoF guidewire tip, with the ability to deliver tension to two orthogonal degrees-of-freedom. We also introduced the design and manufacturing process for such an active guidewire and analyzed the statics and kinematics of the joints that constitute the robot. We demonstrated a control strategy for the base joint of the robot taking advantage of the statics model. Unlike most traditional continuum robots, the two degrees-of-freedom in the guidewire tip are load-coupled, and this coupling must be accounted for by the control strategy. Therefore, in our future work, we plan to build a model for this coupling and account using the same framework as described previously.

References

[1] F. G. R. Fowkes, D. Rudan, I. Rudan, V. Aboyans, J. O. Denenberg, M. M. McDermott, P. E. Norman, U. K. Sampson, L. J. Williams, G. A. Mensah, *et al.*, "Comparison of global estimates of prevalence and risk factors for peripheral artery disease in 2000 and 2010: a systematic review and analysis," *The Lancet*, vol. 382, no. 9901, pp. 1329–1340, 2013.

[2] C. R. Narins, "Access strategies for peripheral arterial intervention," *Cardiol J*, vol. 16, no. 1, pp. 88–97, 2009.

[3] S. M. Grenon, L. M. Reilly, and V. G. Ramaiah, "Technical endovascular highlights for crossing the difficult aortic bifurcation," *Journal of vascular surgery*, vol. 54, no. 3, pp. 893–896, 2011.

[4] A. Ali, D. H. Plettenburg, and P. Breedveld, "Steerable catheters in cardiology: Classifying steerability and assessing future challenges," *IEEE Transactions on Biomedical Engineering*, vol. 63, no. 4, pp. 679–693, 2016.

[5] P. A. York, P. J. Swaney, H. B. Gilbert, and R. J. Webster, "A wrist for needle-sized surgical robots," in *Robotics and Automation (ICRA), 2015 IEEE International Conference on*. IEEE, 2015, pp. 1776–1781.

[6] K. W. Eastwood, H. Azimian, B. Carrillo, T. Looi, H. E. Naguib, and J. M. Drake, "Kinetostatic design of asymmetric notch joints for surgical robots," in *Intelligent Robots and Systems (IROS), 2016 IEEE/RSJ International Conference on*. IEEE, 2016, pp. 2381–2387.

[7] P. M. Loschak, L. J. Brattain, and R. D. Howe, "Algorithms for automatically pointing ultrasound imaging catheters," *IEEE Transactions on Robotics*, vol. 33, no. 1, pp. 81–91, 2017.

[8] P. M. Loschak, A. Değirmenci, and R. D. Howe, "Predictive filtering in motion compensation with steerable cardiac catheters," in *Robotics and Automation (ICRA), 2017 IEEE International Conference on*. IEEE, 2017, pp. 4830–4836.

[9] R. S. Penning, J. Jung, N. J. Ferrier, and M. R. Zinn, "An evaluation of closed-loop control options for continuum manipulators," in *Robotics and Automation (ICRA), 2012 IEEE International Conference on*. IEEE, 2012, pp. 5392–5397.

[10] R. E. Goldman, A. Bajo, and N. Simaan, "Compliant motion control for multisegment continuum robots with actuation force sensing," *IEEE Transactions on Robotics*, vol. 30, no. 4, pp. 890–902, 2014.

[11] D. B. Camarillo, C. F. Milne, C. R. Carlson, M. R. Zinn, and J. K. Salisbury, "Mechanics modeling of tendon-driven continuum manipulators," *IEEE Transactions on Robotics*, vol. 24, no. 6, pp. 1262–1273, 2008.

[12] D. B. Camarillo, C. R. Carlson, and J. K. Salisbury, "Configuration tracking for continuum manipulators with coupled tendon drive," *IEEE Transactions on Robotics*, vol. 25, no. 4, pp. 798–808, 2009.

[13] D. B. Camarillo, K. E. Loewke, C. R. Carlson, and J. K. Salisbury, "Vision based 3-d shape sensing of flexible manipulators," in *Robotics and Automation, 2008. ICRA 2008. IEEE International Conference on*. IEEE, 2008, pp. 2940–2947.

[14] E. J. Lobaton, J. Fu, L. G. Torres, and R. Alterovitz, "Continuous shape estimation of continuum robots using x-ray images," in *Robotics and Automation (ICRA), 2013 IEEE International Conference on*. IEEE, 2013, pp. 725–732.

[15] R. J. Roesthuis and S. Misra, "Steering of multisegment continuum manipulators using rigid-link modeling and fbg-based shape sensing," *IEEE transactions on robotics*, vol. 32, no. 2, pp. 372–382, 2016.

[16] C. Shi, X. Luo, P. Qi, T. Li, S. Song, Z. Najdovski, H. Ren, and T. Fukuda, "Shape sensing techniques for continuum robots in minimally invasive surgery: A survey," *IEEE Transactions on Biomedical Engineering*, 2016.

[17] Y. Kim, S. S. Cheng, and J. P. Desai, "Towards the development of a spring-based continuum robot for neurosurgery," in *Medical Imaging 2015: Image-Guided Procedures, Robotic Interventions, and Modeling*, vol. 9415. International Society for Optics and Photonics, 2015, p. 94151Q.

[18] P. Breedveld, "Steerable laparoscopic cable-ring forceps," *Journal of Medical Devices*, vol. 4, no. 2, p. 027518, 2010.

[19] R. J. Webster III and B. A. Jones, "Design and kinematic modeling of constant curvature continuum robots: A review," *The International Journal of Robotics Research*, vol. 29, no. 13, pp. 1661–1683, 2010.

[20] G. J. Vrooijink, A. Denasi, J. G. Grandjean, and S. Misra, "Model predictive control of a robotically actuated delivery sheath for beating heart compensation," *The International Journal of Robotics Research*, vol. 36, no. 2, pp. 193–209, 2017.

[21] G. J. Vrooijink, T. T. Ellenbroek, P. Breedveld, J. G. Grandjean, and S. Misra, "A preliminary study on using a robotically-actuated delivery sheath (rads) for transapical aortic valve implantation," in *Robotics and Automation (ICRA), 2014 IEEE International Conference on*. IEEE, 2014, pp. 4380–4386.

[22] B. Siciliano, L. Sciavicco, L. Villani, and G. Oriolo, "Robotics: modelling, planning and control, ser. advanced textbooks in control and signal processing," *Springer*, vol. 26, p. 29, 2009.